

Analytical Models for Predicting the Formation Resistivity Factor and Resistivity Index at Overburden Conditions

Meysam Nourani*, Stefano Pruno, Mohammad Ghasemi, Muhamet Meti Fazlija, Byron Gonzalez and Hans-Erik Rodvelt

Stratum Reservoir AS, Stavanger, Norway

Abstract. In this study, new parameters referred to as rock resistivity modulus (RRM) and true resistivity modulus (TRM) were defined. Analytical models were developed based on RRM, TRM and Archie's equation for predicting Formation Resistivity Factor (FRF) and Resistivity Index (RI) under overburden pressure conditions. The results indicated that overburden FRF is dependent on FRF at initial pressure (ambient FRF), RRM and net confining pressure difference. RRM decreases with cementation factor and rock compressibility. The proposed FRF model was validated using 374 actual core data of 79 plug samples (31 sandstone and 48 carbonate plug samples) from three sandstone reservoirs and four carbonate reservoirs, measured under 4-6 different overburden pressures. The developed FRF model fitted the experimental data with average relative error of 2% and 3% for sandstone and carbonate samples respectively. Moreover, the applications and limitations of the models have been investigated and discussed. Further theoretical analysis showed that overburden RI is a function of RI at initial pressure, TRM and net confining pressure difference. The developed models supplement resistivity measurements and can be applied to estimate FRF, RI and saturation exponent (n) variations with overburden pressure.

Introduction

Archie's Formation Resistivity Factor (FRF) is one of the most essential petrophysical properties for log calibration and reservoir characterisation. The FRF is a dimensionless parameter defined as the ratio of the resistivity of rock fully saturated with brine (R_o [Ωm]) to the formation water resistivity (R_w [Ωm]). FRF is related to the porosity (ϕ [fraction]) by the Archie equation as follows:

$$FRF = \frac{R_o}{R_w} = \phi^{-m} \quad (1)$$

where m is the cementation factor which is also referred to as porosity exponent or cementation exponent.

The porosity of rock is the ratio between the pore space volume (V_p) to the bulk volume (V_b) of the rock and is expressed as a fraction. Considering electrical properties of rocks, the Resistivity Index (RI) is the second essential dimensionless parameter. RI is calculated as the ratio of the resistivity of rock when partially saturated with water (R_t [Ωm]) to the R_o . It is linked to the water saturation (S_w [fraction]), as follows:

$$RI = \frac{R_t}{R_o} = S_w^{-n} \quad (2)$$

where n is the saturation exponent [1]. Combining Equations (1) and (2) yields the following equation which is referred to as saturation equation:

$$S_w = \left(\frac{R_w}{\phi^m R_t} \right)^{\frac{1}{n}} \quad (3)$$

These empirical equations were derived for clean, clay-free, strongly water-wet sandstones with simple and unimodal pore geometry. Further assumptions are that the rock grains are non-conductive, and all the water contributes to electrical current flow [2–4]. The estimation of the volume of hydrocarbon initially in place at reservoir conditions ($HCIP$ [m^3]) is vital information for reservoir management and is determined by the water saturation, the porosity, and the volume of the reservoir (V [m^3]), as follows [5,6]:

$$HCIP = V\phi(1 - S_w) \quad (4)$$

The accuracy of predicting the volume of the reservoir is high for mature fields which have been produced through numerous wells for many years. In addition, reservoir porosity can be obtained by using logging tools, such as sonic and neutron devices. Calibrating logging data to core analysis results can provide more accurate data sets and increase confidence in estimated reservoir porosity values.

Various methodologies for obtaining R_w have been reported in literature, such as direct measurement in a resistivity cell, chemical analysis of produced water samples, use of spontaneous potential (SP) curves, water catalogues and numerous other empirical methods [7–10]. Moreover, R_t can be achieved from the electrical resistivity logs. Therefore, by determining Archie's exponents (m and n) through conducting laboratory measurements, the in-situ water saturation can be calculated using Equation (3). These empirical parameters must be obtained at representative pressure and temperature conditions. Hence, they are quantified based on the results of special core analysis (SCAL). Laboratory FRF SCAL tests are performed in such a way as to be as representative as possible of the reservoir

* Corresponding author: meysam.nourani@stratumreservoir.com

conditions, but typically they are performed at lower temperature and overburden pressure conditions. This is due to time constraints, the complexity of the measurements and higher expense. It is also common to perform FRF tests at a single overburden pressure due to limited SCAL program budget [11]. Thus, testing conditions are usually dissimilar to the actual conditions in the reservoir.

Overburden pressure is defined as the vertical stress or hydrostatic pressure exerted by all overlying layers of material (rock, salt, water) on a reference point or layer. The formation compresses once the overburden pressure increases beyond the limit of the fluid pressure in the pore space [12]. As a result of compression, the tortuosity of flow paths varies and the pore sizes and accordingly porosity, decreases. As porosity decreases, in accordance with Archie's law, FRF increases [13–16]. Many researchers have investigated the effect of confining pressure on the FRF of numerous rock samples. It has been reported convincingly that FRF increases with increasing confining stress and overburden pressure [13–24]. The effect of overburden pressure on FRF is dissimilar for different rocks depending on the pore size distribution, clay content, porosity, and permeability [8].

Since determination of cementation and saturation exponents is among the most uncertain parameters required for estimating *HCIIP* in Equation (4), without considering the effect of overburden pressure, the predicted saturation from resistivity logs can be a basis of uncertainties and subsequently leads to inaccurate estimations of hydrocarbon volumes initially in place.

To model the effect of overburden pressure in sandstone and carbonate cores a novel, theoretical investigation supported by experimental results is introduced. The objectives of this analytical-experimental research are to explore the relationship between FRF, RI and overburden pressure and to develop mathematical models for predicting FRF under different overburden pressures. The models are validated using actual core sample resistivity data at ambient temperature and different net confining pressure conditions from sandstone and carbonate reservoirs.

Development of the FRF Models

Rock resistivity modulus (RRM) is defined as the change in R_o per unit of R_o per change in pressure. Thus, RRM is a measure of the relative change in the rock resistivity of rock fully saturated with brine in response to a pressure change as follows:

$$\gamma_{R_o} = -\frac{1}{R_o} \frac{\partial R_o}{\partial P} \quad (5)$$

In addition, the water resistivity modulus (WRM) and the true resistivity modulus (TRM) can be defined by analogy to RRM as follows:

$$\gamma_{R_w} = -\frac{1}{R_w} \frac{\partial R_w}{\partial P} \quad (6)$$

$$\gamma_{R_t} = -\frac{1}{R_t} \frac{\partial R_t}{\partial P} \quad (7)$$

By separating the R_o in Equation (5) and integrating while assuming a constant RRM over the pressure interval of interest, the R_o at a given overburden pressure can be calculated as follows:

$$R_{o_2} = R_{o_1} e^{-\gamma_{R_o} \Delta P} \quad (8)$$

where R_{o_1} and ΔP are rock resistivity at initial pressure and net confining pressure difference respectively. Combining Equations (1) and (5), yields the following equation:

$$\gamma_{R_o} = -\frac{\varphi^m}{R_w} \frac{\partial (\frac{R_w}{\varphi^m})}{\partial P} \quad (9)$$

It has been shown that the variations in cementation and saturation exponents with overburden pressure are not significant [11,24,25]. The maximum change in the cementation and saturation exponents with overburden pressure for water-wet cores have been reported at around 2% and 8% respectively [24]. Hence, for the sake of simplicity in deriving the mathematical models, it was supposed that m and n coefficients do not vary with overburden pressure. Accordingly, by assuming a constant cementation exponent over the pressure interval of interest, taking the derivative of the term $(\frac{R_w}{\varphi^m})$ with respect to pressure in Equation (9) and rearranging it, the RRM can be calculated using the following formula:

$$\gamma_{R_o} = -\frac{1}{R_w} \frac{\partial R_w}{\partial P} + m \frac{1}{\varphi} \frac{\partial \varphi}{\partial P} \quad (10)$$

The variations in porosity of a porous rock due to changes in overburden pressure are related to the pore volume compressibility (C_p) and bulk compressibility (C_b) which are expressed in Equations (11) and (12) [26]:

$$C_p = -\frac{1}{V_p} \frac{\partial V_p}{\partial P} \quad (11)$$

$$C_b = -\frac{1}{V_b} \frac{\partial V_b}{\partial P} \quad (12)$$

Taking the derivative of the porosity with respect to pressure and replacing C_p and C_b from Equations (11) and (12) into it, yields the following equation:

$$\frac{\partial \varphi}{\partial P} = \varphi (C_b - C_p) \quad (13)$$

By combining Equations (6), (10) and (13), the following equation can be obtained:

$$\gamma_{R_o} = \gamma_{R_w} + m (C_b - C_p) \quad (14)$$

The water resistivity is independent of pressure, for pressure and temperature conditions below 58,000 psi (4,000 bar) and 170 °C. [27]. This pressure is much greater than those normally encountered in hydrocarbon reservoirs. Consequently, the water resistivity and WRM over the pressure interval of interest are assumed constant and zero respectively. By dividing both sides of Equation (8) by the water resistivity, the overburden FRF can be calculated as:

$$FRF_2 = FRF_1 e^{-\gamma_{R_o} \Delta P} \quad (15)$$

In addition, by disregarding WRM in Equation (14), a simplified formula for estimating the RRM is obtained:

$$\gamma_{R_o} = m (C_b - C_p) \quad (16)$$

By replacing the RRM in Equation (15), the FRF at a given overburden pressure can be calculated as follows:

$$FRF_2 = FRF_1 e^{m(C_p - C_b)\Delta P} \quad (17)$$

Thus, FRF can be predicted by two models. Measuring FRF under several overburden pressures is an essential requirement for applying the first model which is referred to as the Multi-FRF model. In the Multi-FRF model, Equation (15) is used to fit overburden FRF data. A plot of the ratio $\frac{FRF_2}{FRF_1}$ versus the net confining pressure difference on a semi-logarithmic scale passing through $\Delta P = 0$, when $FRF_2 = FRF_1$, gives a straight line of slope $-\gamma_{R_o}$, as:

$$\gamma_{R_o} = - \frac{\ln \frac{FRF_2}{FRF_1}}{\Delta P} \quad (18)$$

The obtained RRM can be used to predict FRF at any overburden pressure using Equation (15). When FRF is measured only at initial pressure, the second model which is referred to as the Single-FRF model can be used to estimate overburden FRF through Equation (17). It should be noted that the FRF models have been derived based on Archie's equation, thus Archie's assumptions apply to them. Accordingly, the developed FRF models are applicable only if Archie's equation is valid.

Validating the FRF Models

Two overburden FRF datasets comprising samples from three sandstone and four carbonate reservoirs were used to apply and validate the developed models. The first dataset includes 55 plug samples from five different North Sea reservoirs. The range of porosity, permeability and grain density of the samples have been investigated and listed in Table 1. Bulk mineral composition of the samples was measured by X-ray diffraction (XRD). The average tectosilicates, carbonate and phyllosilicate content of the samples are presented in Table 2.

Table 1. Overview of the range of porosity, water permeability (K_w), grain density of the samples.

Reservoir	Porosity (%)		Kw (mD)		Grain density (g/cc)	
	Min.	Max.	Min.	Max.	Min.	Max.
1	17.1	43.4	0.012	6.51	2.68	2.71
2	25.5	39.8	0.012	2.86	2.65	2.71
3	18.0	27.3	0.503	571	2.64	2.77
4	16.4	35.9	0.338	980	2.62	2.69
5	31.4	40.4	592	3890	2.65	2.79

Table 2. Overview of the average bulk mineral composition.

Reservoir	Tectosilicates (wt%)	Carbonates (wt%)	Phyllosilicates (wt%)
1	1	99	0
2	20	77	1
3	73	16	5
4	78	2	17
5	73	13	5

Equations (15) and (17) were fitted to the measured FRF data, and Figures 1 and 2 show examples of the best regression line and least square method statistical parameters. After applying the proposed models to the dataset, an excellent agreement has been observed ($R^2=0.9992$) between both the Multi-FRF and Single-FRF models and the measured data (Figure 1).

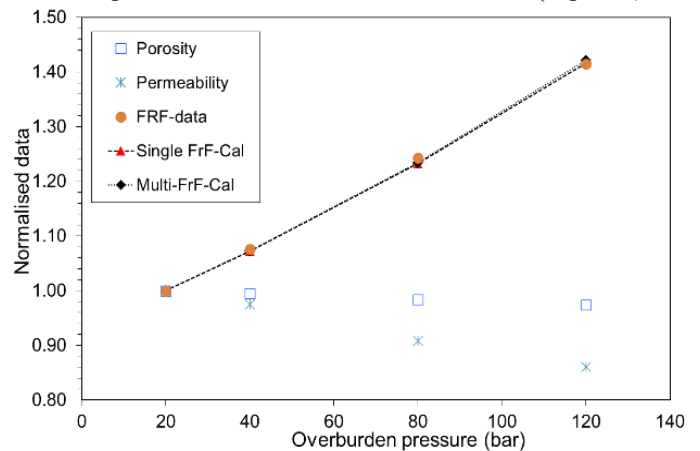


Fig. 1. Example 1, fitting of Equations (15) and (17) to FRF data; relation between the overburden pressure and normalized porosity, permeability and FRF.

Figure 2 shows a very good correlation with the Multi-FRF model ($R^2=0.9973$), whereas uncertainty in compressibility data causes the Single-FRF model to overestimate the FRF values at overburden pressures above the initial pressure. Although, the Single-FRF model has clearly deviated from the measured data, the maximum relative error between the measured and predicted FRF at 120 bar is only 12.6% as shown in Figure 2.

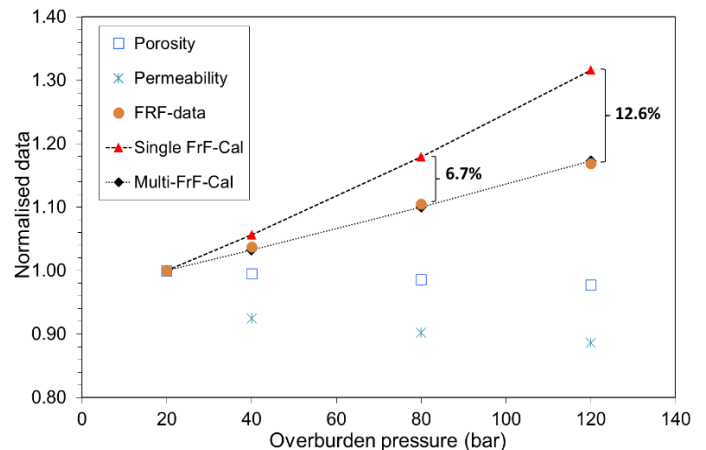


Fig. 2. Example 2, fitting of Equations (15) and (17) to FRF data; relationship between the overburden pressure and normalized porosity, permeability and FRF.

$\ln \frac{FRF_2}{FRF_1}$ is plotted versus the net confining pressure difference for six sandstone samples in Figure 3. As examples, the RRM_s were calculated from the slope of the lines in Figure 3 and listed in Table 3. As R_o increases with overburden pressure, the gradient of rock resistivity with respect to pressure becomes a positive number. Thus, according to Equation (5), RRM is a negative number as shown in Table 3.

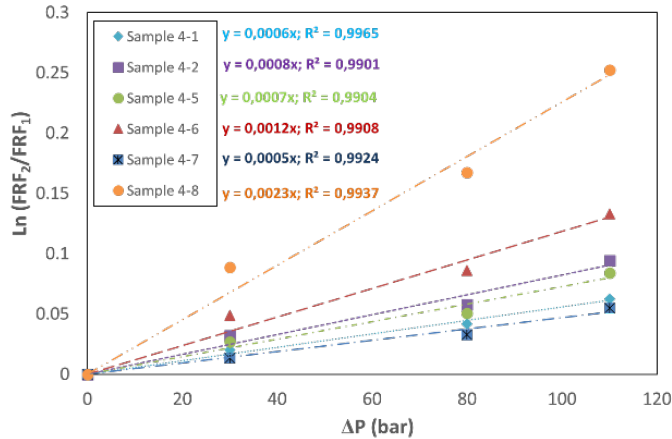


Fig. 3. $\ln \frac{FRF_2}{FRF_1}$ versus net confining pressure difference. According to Equation (18), the RRM_s were determined by the slope of lines for six North Sea samples.

Table 3. The calculated RRM_s from the slope of the lines in Fig.3.

Sample	FRF ₁ @ 20 bar	RRM (bar ⁻¹)
4-1	6.80	-5.57E-04
4-2	10.13	-8.21E-04
4-5	7.97	-7.27E-04
4-6	12.55	-1.18E-03
4-7	6.67	-4.68E-04
4-8	18.30	-2.26E-03

The modelled overburden FRF calculated by the Multi-FRF method is plotted versus the measured overburden FRF of the 55 samples from five North Sea reservoirs in Figure 4. A good fit between the model-predicted overburden FRF and the experimental measured laboratory data is observed.

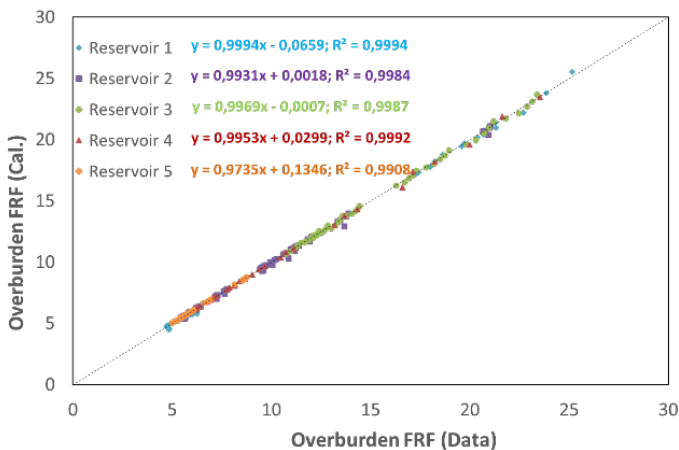


Fig. 4. Overburden FRF calculated using Equation (15) versus measured overburden FRF for five North Sea reservoirs.

The R² calculated by Single-FRF and Multi-FRF models for North Sea reservoirs are listed in Table 4. As expected, the Multi-FRF model shows a higher degree of accuracy than the Single-FRF model.

Table 4. Overview of the corresponding R² from model equations.

Reservoir	R ² (Single-FRF)	R ² (Multi-FRF)
1	0.9961	0.9994
2	0.9996	0.9984
3	0.9949	0.9987
4	0.9968	0.9992
5	0.9767	0.9908

The second dataset has been extracted from published literature [28,29] and includes 24 plug samples from two carbonate reservoirs. Figure 5 shows that the estimated overburden FRF from Equation (15) correlates with the experimental data for six samples from field S [28] with a maximum relative error of less than 8%.

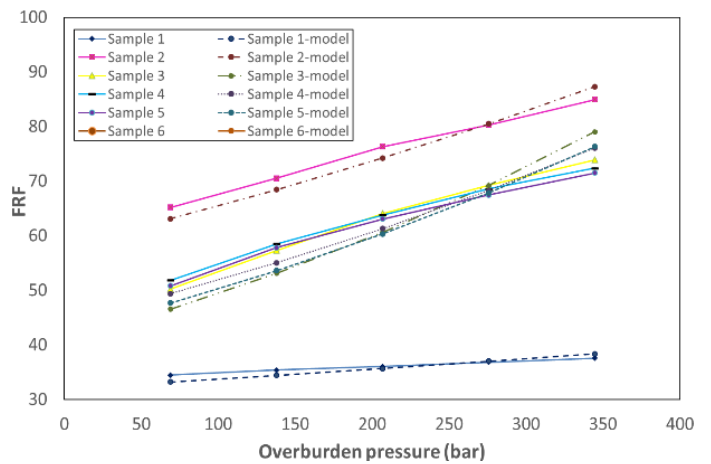


Fig. 5. Measured and calculated overburden FRF by Multi-FRF model versus overburden pressure for six samples from field S [28].

Figure 6 indicates a good correlation between the Multi-FRF model predicted and the measured overburden FRF data, with R² of 0.9869 and 0.9970 for the data from literature [28,29].

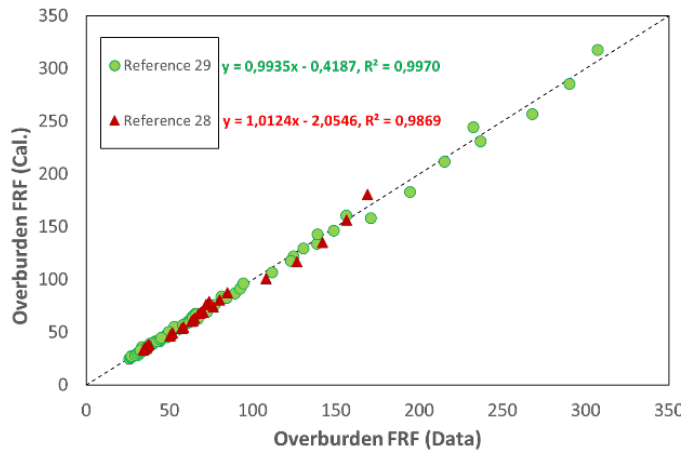


Fig. 6. Overburden FRF calculated using Equation (15) versus measured overburden FRF for two carbonate reservoirs [28,29].

As presented by Figure 7, a very good correlation is seen between the Multi-FRF model estimated values and the measured data. For overburden FRF, R^2 values are higher than 0.9975 for 153 sandstone and 221 carbonate data points.

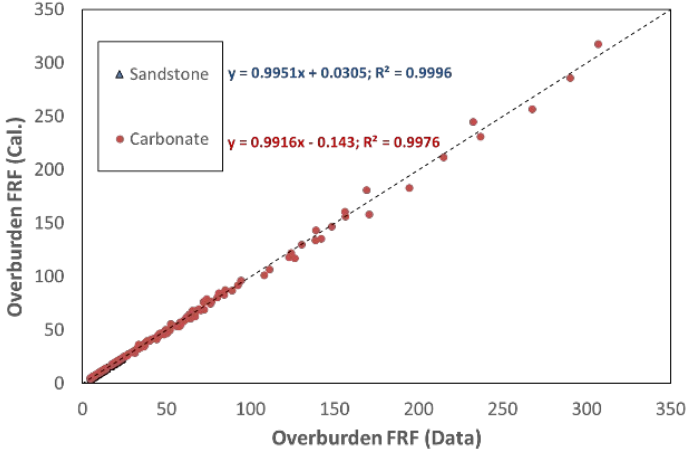


Fig. 7. Overburden FRF calculated using Equation (15) versus measured overburden FRF for sandstone and carbonate reservoirs.

Moreover, the average relative error for the 31 sandstone and 48 carbonate samples were calculated at 2% and 3% respectively. Overall, these results indicate that the general trend of the Multi-FRF model demonstrates very good correlation with the laboratory measurements for all the 79 sandstone and carbonate samples.

Development of the RI Model

A similar modelling approach can be applied to the calculation of RI and Archie's saturation n -exponent. If R_t is separated in Equation (7) and integrated while assuming TRM is constant over the pressure interval of interest, the overburden R_t can be obtained from Equation (19):

$$R_{t_2} = R_{t_1} e^{-\gamma_{R_t} \Delta P} \quad (19)$$

By dividing Equation (19) by Equation (8), the RI at a given overburden pressure can be predicted as follows:

$$RI_2 = RI_1 e^{(\gamma_{R_o} - \gamma_{R_t}) \Delta P} \quad (20)$$

Combining Equations (1), (2) and (7) yields the following equation:

$$\gamma_{R_t} = -\frac{\varphi^m S_w^n}{R_w} \times \frac{\partial(\frac{R_w}{\varphi^m S_w^n})}{\partial P} \quad (21)$$

Hence, by assuming constant cementation and saturation exponents over the pressure interval of interest and taking the derivative of the term $(\frac{R_w}{\varphi^m S_w^n})$ with respect to pressure in Equation (21) and rearranging it, the TRM can be calculated as follows:

$$\gamma_{R_t} = -\frac{1}{R_w} \frac{\partial R_w}{\partial P} + m \frac{1}{\varphi} \frac{\partial \varphi}{\partial P} + n \frac{1}{S_w} \frac{\partial S_w}{\partial P} \quad (22)$$

In addition, the formation brine compressibility; C_{fb} , is expressed as follows [30]:

$$C_{fb} = -\frac{1}{V_w} \frac{\partial V_w}{\partial P} \quad (23)$$

where V_w is the volume of the formation brine; this volume can be estimated through Equation (24).

$$V_w = \varphi V_b S_w \quad (24)$$

Combining Equations (23) and (24) and taking the derivative of the term $(\varphi V_b S_w)$ with respect to pressure and replacing C_p and C_b from Equations (11) and (12) into it, yields the following equation:

$$\frac{1}{S_w} \frac{\partial S_w}{\partial P} = C_p - C_{fb} \quad (25)$$

Thus, the TRM can be calculated by replacing Equations (6), (13) and (25) into Equation (22) as below:

$$\gamma_{R_t} = \gamma_{R_w} + m(C_b - C_p) + n(C_p - C_{fb}) \quad (26)$$

By replacing the RRM and TRM (from Equations (14) and (26) respectively) in Equation (20), the overburden RI can be calculated as follows:

$$RI_2 = RI_1 e^{n(C_{fb} - C_p) \Delta P} \quad (27)$$

From integration of Equation (25) with respect to pressure, the S_w at a given overburden pressure can be predicted as follows:

$$S_{w_2} = S_{w_1} e^{(C_p - C_{fb}) \Delta P} \quad (28)$$

Consequently, the saturation exponent at a given overburden pressure can be predicted by replacing Equations (27) and (28) into Equation (2) as below:

$$n_2 = -\frac{\ln RI_1 + [n_1 (C_{fb} - C_p)] \Delta P}{\ln S_{w_1} + (C_p - C_{fb}) \Delta P} \quad (29)$$

The compressibility of formation brine [psi^{-1}] containing no gas in solution and for pressures from 1,000 to 20,000 psi (69 to 2,844 bar), temperatures between 200 and 270°F (93 and 132°C) and salinities of 0 to 200 g/L NaCl equivalent can be estimated using the following correlation [30]:

$$C_{fb} = \frac{1}{7.033 P + 541.5 C - 5377 T + 403.3 \times 10^3} \quad (30)$$

where P , C and T are pressure [psi], salt concentration [g/L] and temperature [$^{\circ}\text{F}$] respectively. The more general forms of the Equations (27), (28) and (29) result from replacing the pressure steps 1 and 2 with i and $i + 1$ ($i \geq 1$), so:

$$RI_{i+1} = RI_i e^{n_i (C_{fb_i} - C_{p_i}) (P_{i+1} - P_i)} \quad (31)$$

$$S_{w_{i+1}} = S_{w_i} e^{(C_{p_i} - C_{fb_i}) (P_{i+1} - P_i)} \quad (32)$$

$$n_{i+1} = -\frac{\ln RI_i + n_i (C_{fb_i} - C_{p_i}) (P_{i+1} - P_i)}{\ln S_{w_i} + (C_{p_i} - C_{fb_i}) (P_{i+1} - P_i)} \quad (33)$$

Figure 8 illustrates an example of predicting saturation exponents at various overburden pressures using Equations (31), (32) and (33). The composite n-exponent was equal to 1.93 and was calculated from measurements conducted at 190 bar and 98°C on 12 SCAL plug samples from reservoir 3. The composite saturation exponents for net confining overburden pressures of 350 and 700 bar are predicted as 1.95 and 1.97 respectively.

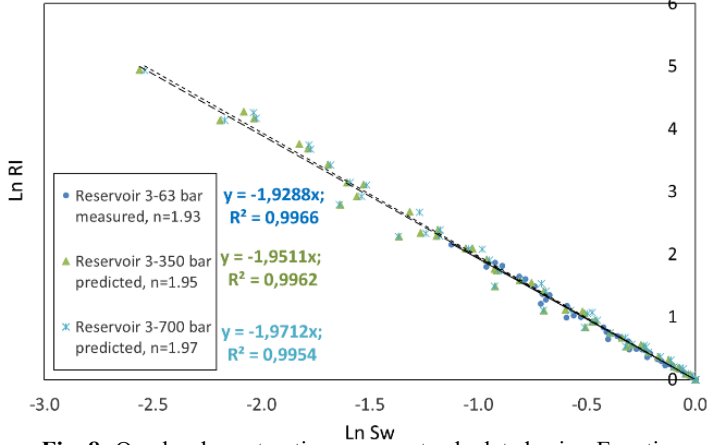


Fig. 8. Overburden saturation exponent calculated using Equations (31), (32) and (33).

Figure 9 shows the predicted composite n-exponent for reservoirs 1-4 versus overburden pressure (RI data is not available for reservoir 5). Linear relationships between the predicted composite saturation exponents and the overburden pressures have been developed. Saturation exponent increases linearly with overburden pressure, as shown in Figure 9.

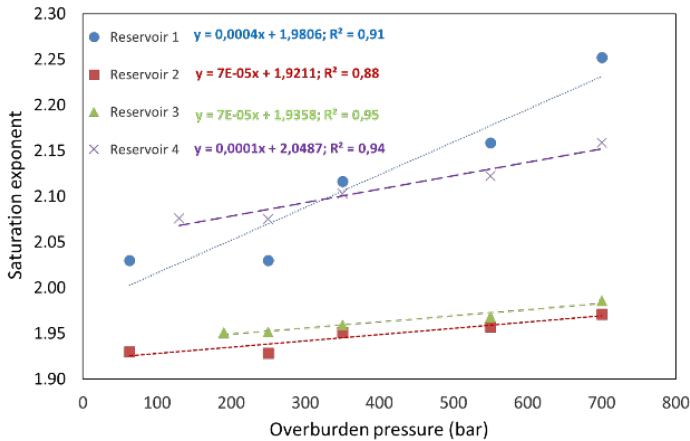


Fig. 9. Predicted composite n-exponent versus overburden pressure for reservoirs 1, 2, 3 and 4.

As shown in Table 2, reservoirs 2 and 3 are predominately carbonate and silicate reservoirs, respectively. The minimum rate of change in saturation exponent with respect to overburden pressure are observed for these two reservoirs with different lithologies (Figure 9). Also, the maximum gradient of saturation exponent with respect to overburden pressure is calculated for reservoir 1 which is the nearly pure (99%) carbonate reservoir. According to Equation (33), saturation exponent is dependent on the difference between the formation brine compressibility and the pore volume compressibility. When C_{fb} and C_p are almost identical and

consequently their difference is close to zero, the saturation exponent doesn't change significantly. Lewis et al. reported that changes in overburden pressures have a relatively minor effect upon the saturation exponent, but at the same time it slightly rises as the overburden pressure increases [24]. Although, experimental data was not available to support the theoretically developed model, but the predicted trends show consistency with the reported results by Lewis et al.

Development of the Apparent FRF Model

Conductivity is defined as the reciprocal of the electrical resistivity. Clay minerals in a rock play a role as a separate conductor. The effect of the clay on the conductivity of the rock is dependent upon the type, quantity, structure, and distribution in the rock [4]. As can be seen from the Table 2, the amount of clay in the investigated sandstone samples is low and varies between 0% and 17%. Figure 10 shows the conductivity behaviour of the shaly-sand as a function of brine conductivity, where C_w [$\Omega^{-1}m^{-1}$] and C_o [$\Omega^{-1}m^{-1}$] are the brine conductivity and the brine-saturated rock conductivity, respectively. The C_o is related to the C_w by the Waxman and Smits equation as follows [31]:

$$C_o = \frac{C_w}{F^*} + \frac{BQ_v}{F^*} \quad (34)$$

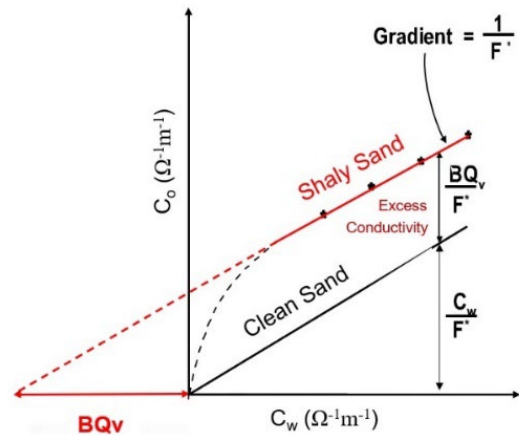


Fig. 10. Water-saturated rock conductivity (C_o) as a function of water conductivity (C_w). Adopted from [31].

where F^* , B [$(\Omega^{-1}m^{-1})/(meq/ml)$] and Q_v [meq/ml] are the shaly-sand FRF (apparent FRF), the volume concentration of sodium exchange cations associated with the clay and the equivalent conductance of sodium clay exchange cations, respectively. Therefore, as shown in Figure 10, beyond the primary dilute area, C_o increases linearly with C_w . The term $(\frac{BQ_v}{F^*})$ is determined from the intercept of the regressed best-fit straight-line curve to the C_o - C_w data pairs [11]. The reciprocal of the shaly-sand FRF is calculated from the gradient (slope) of the plot C_o as a function of C_w as [31,32]:

$$\frac{1}{F^*} = \frac{dC_o}{dC_w} \quad (35)$$

By assuming that brine conductivity is independent of pressure and taking the derivative of Equation (35) with respect to pressure, yields the following equation:

$$\frac{\partial F^*}{\partial P} = -\frac{\frac{\partial(dC_o)}{\partial P} dC_w}{dC_o dC_o} \quad (36)$$

The rock conductivity modulus (RCM) can be defined as follows:

$$\gamma_{C_o} = -\frac{1}{dC_o} \frac{\partial(dC_o)}{\partial P} \quad (37)$$

Combining Equations (35), (36) and (37), yields the following equation:

$$\frac{\partial F^*}{F^*} = \gamma_{C_o} \partial P \quad (38)$$

From integration of Equation (38) with respect to pressure while assuming a constant RCM over the pressure interval of interest, the apparent FRF at overburden pressure can be calculated from Equation (39) as follows:

$$F^*_2 = F^*_1 e^{\gamma_{C_o} \Delta P} \quad (39)$$

For clean sands, excess conductivity which is the intercept of the line ($\frac{BQ_v}{F^*}$) in Figure 10 becomes zero. Thus, RCM can be simplified as below:

$$\gamma_{C_o} = -\frac{1}{C_o} \frac{\partial C_o}{\partial P} \quad (40)$$

Replacing the brine-saturated rock conductivity ($R_o = \frac{1}{C_o}$) in RRM's definition in Equation (5) and taking the derivative with respect to pressure and combining it with Equation (40), yields $\gamma_{R_o} = -\gamma_{C_o}$. As mentioned before, RRM values are negative since rock resistivity increases with overburden pressure. As the rock conductivity of clean sand is the reciprocal of the rock resistivity, the rock conductivity decreases with overburden pressure. Consequently, according to Equation (40), RCM becomes positive normally. Consequently, for clean sands, Equations (15) and (39) match as expected as the apparent FRF approaches FRF, and power coefficients reflect equal values. Figure 11 shows an example of predicting apparent FRF at different overburden pressures.

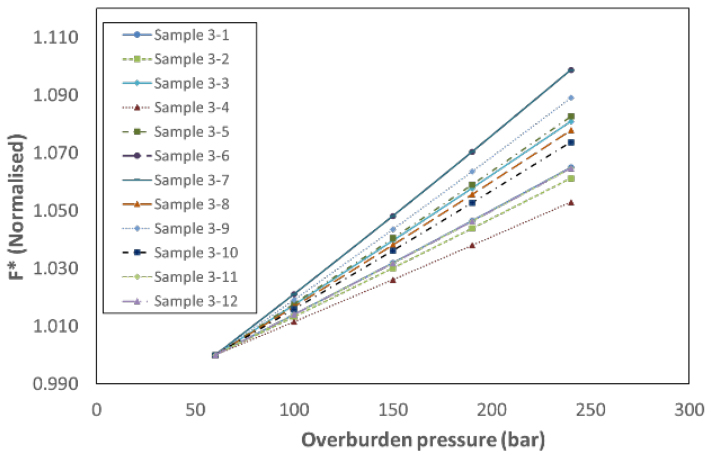


Fig. 11. Example predicting apparent FRF for 12 SCAL plug samples from reservoir 3, using Equation (39).

The apparent FRF data at stress are normalised to values at 60 bar for 12 samples from reservoir 3, as shown in Figure 11. Overburden FRF measurement has been conducted at

several overburden pressures on reservoir 3 samples, whereas C_o/C_w measurements have been performed only at one overburden pressure step. According to Table 2, the clay content of reservoir 3 samples is quite low. Thus, the absolute values of RRM and RCM can be assumed equal. The apparent FRF at 190 bar and 20°C was calculated based on the C_o/C_w measurement. The apparent FRF is predicted at overburden pressures of 60, 100, 150 and 240 bar, using Equation (39) and RRM obtained from the overburden FRF measurement.

Results and Discussion

A good correlation was observed between exponential models presented in equations (15) and (17) and FRF experimental results in Figure 1; also, for the investigated dataset the graphical trends appear to be a linear function of the increasing overburden pressure. This is mathematically reasonable as the power coefficients in Equation (15) and (17) are much less than one, thus the exponential function can be converted to a linear function as follows:

$$FRF_2 = aP_2 + b \quad (41)$$

where a and b are the slope and the intercept of the line, respectively as:

$$a = FRF_1 m_1 (C_p - C_b) \quad (42)$$

$$b = FRF_1 [1 - m_1 P_1 (C_p - C_b)] \quad (43)$$

As ΔP and consequently the power coefficients increase by pressure, the prerequisite condition needed for converting exponential function to linear function ($-\gamma_{R_o} \Delta P \ll 1$) becomes invalid. Accordingly, deviations from linearity between the FRF and the overburden pressure are observed for high pressures. Figures 12 and 13 illustrate examples of this behavior of the fitting of the Multi-FRF model to the FRF data measured at a high range of overburden pressure.

The effect of overburden pressure on the electrical resistivities has been attributed to the mechanical feature which comprises pore constriction alterations and pore volume deformations [16]. The grain framework compacts and deforms from an increase in overburden pressure and because of compaction. Framework grains become in inlaid contact with each other, instead of being in point or line contact [33].

Once a rock is exposed to overburden pressure, it experiences a variation in volume. This variation is called strain [34]. Until strain is proportional to the magnitude of the applied pressure, the rock shows elastic behaviour. Under such conditions if the pressure is removed, the volume of the rock sample returns to its original state. Plastic deformation occurs once the applied overburden pressure on a rock is beyond its elastic limit. Thus, plastic deformation is that deformation that generates a permanent alteration in the volume of a rock without that rock having failed by fracturing [35]. Sudden downward changes in the slope of the plot FRF as a function of overburden pressure at high overburden pressures could be related to the change from more elastic to more plastic or ductile failure behaviour (Figure 12).

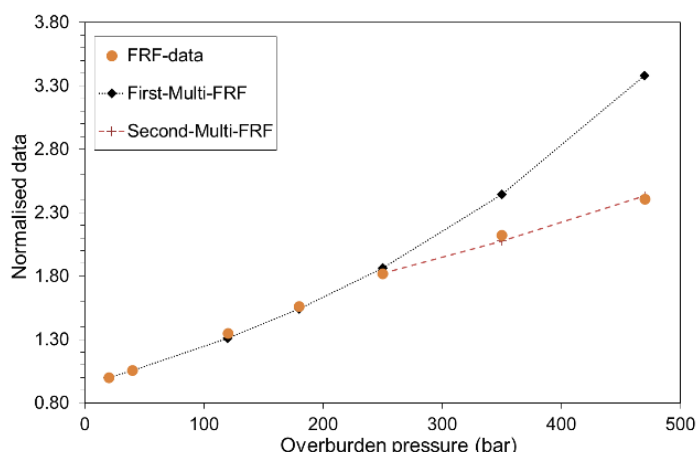


Fig. 12. Example fitting of Equation (15) to the normalised FRF data measured at a large range of overburden pressures when FRF shows a curving downward behaviour.

Micron-scale deformation mechanisms such as grain rotation and sliding, microcrack growth and closure, cement breakage, elastic grain-contact spreading and crystal plastic deformation in clay appear when the applied overburden pressure increases, and the load-bearing grain framework of the sample is extremely high [36]. Abrupt upward changes in the slope of the plot FRF as a function of overburden pressure at very high overburden pressures are indicative of suspected pore collapse, which causes grain rearrangement and repacking (Figure 13).

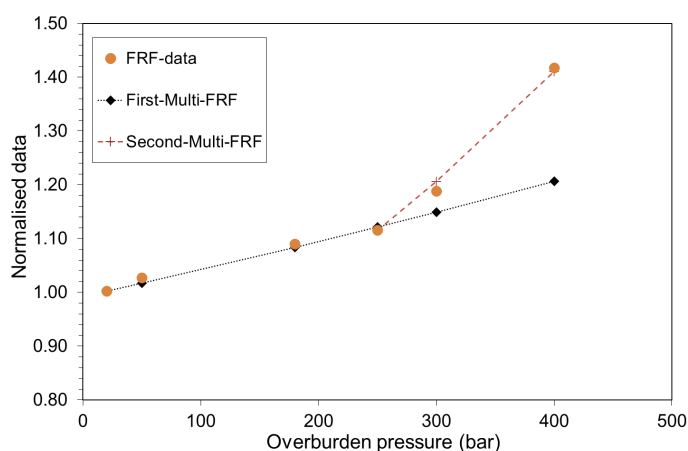


Fig. 13. Example fitting of Equation (15) to the normalised FRF data measured at a large range of overburden pressures when FRF shows curving upward behaviour [11].

When the confining compaction stress is sufficiently high, inelastic mechanisms such as intragranular cracks (contact spalling), grain rotation and grain sliding triggered by intergranular microcracks, and cement breakage are activated and dominated [11,36,37].

Upward or downward changes in the slope of the plot FRF as a function of overburden pressure leads to variation of the original trend of the FRF with the overburden pressure. This consequently causes deviations between the measured FRF data and the proposed model.

To improve the accuracy of the Multi-FRF model in predicting FRF data at a large range of overburden pressures, the second Multi-FRF model can be applied. It may be applied from the point that the trend of the graph of FRF

versus overburden pressure has started to change due to probable plastic behaviour (curving downward behaviour) or rearranged grains and pore structures (curving upward behaviour). Hence, due to the slope change at high overburden pressures, the first Multi-FRF models were not capable of predicting overburden FRFs properly for high overburden pressures in Figures 12 and 13. Moreover, Figures 12 and 13 display the second Multi-FRF models correlate well to the measured FRF data at high overburden pressures. The initial pressure has been set to 250 bar for the second Multi-FRF model in Equation (15); RRM has been calculated based on the FRF values measured at overburden pressures greater than and equal to 250 bar in Figures 12 and 13. R^2 of the plot $\ln \frac{FRF_2}{FRF_1}$ versus the net confining pressure

difference is a good diagnostic tool to verify the requirement of applying the second Multi-FRF model. As shown in Figure 3, R^2 greater than 0.9900 shows that the original trend of the FRF with the overburden pressure works accurately. Whereas R^2 lower than 0.9900 indicates that applying the second Multi-FRF model is most likely needed for more accurate predictions of FRF values at high overburden pressures.

Practically, FRF data at various overburden pressures are not always available. Porosity and water permeability measurements are the basic experiments that are usually measured on all the samples at initial pressure, normally 20 bar, before conducting any SCAL program. FRF can also be measured at initial pressure in conjunction with porosity and water permeability measurements for all the SCAL samples. According to Equation (17), in addition to initial FRF data, the difference between the pore volume compressibility and bulk compressibility is required for predicting overburden FRF by the Single-FRF model. If porosity has been measured under different overburden pressures, C_p-C_b can be estimated through Equation (13). When overburden porosity and compressibility data are not available, C_p can be calculated through empirical correlations such as the following equations [38]:

$$C_p = \frac{97.32 \times 10^{-6}}{(1+55.8721\varphi)^{1.42859}} \quad (44)$$

$$C_p = \frac{0.853531}{(1+2.47664 \times 10^6 \varphi)^{0.9299}} \quad (45)$$

Equations (44) and (45) were developed for consolidated sandstones and limestone, respectively. Also, the bulk compressibility can be related to the pore compressibility as follows [39,40]:

$$C_b \cong C_p \varphi \quad (46)$$

Consequently, the difference between the pore volume compressibility and bulk compressibility can be estimated through Equations (44), (45) and (46). Table 5 demonstrates the sensitivity of using the different methods and data to estimate C_p-C_b and overburden FRF for the sample plotted in Figure 2 at 120 bar where the maximum deviation from the measured FRF data has been observed. Using two overburden porosity values to calculate C_p-C_b through equation 13 leads to a 12.6% overestimation of FRF at 120 bar as shown in Figure 2 and listed in Table 5. Increasing the number of

overburden porosity values to four in calculation of C_p-C_b leads to a 10.3% underestimation of overburden FRF. That means the absolute value of the relative error improves 2.3% by using four overburden porosity values. Whereas using correlations (44), (45) and (46) for estimating C_p-C_b worsens the absolute value of the FRF relative error only 3.1%. The average relative error for predicting overburden FRF for samples from North Sea reservoirs by using the Single-FRF model and correlations (Equations 44-46) is less than 5%. Therefore, although it was shown that the Multi-FRF model is more accurate for predicting FRF in comparison with the Single-FRF model, the Single-FRF model can be applied for predicting overburden FRF if the prerequisites of the Multi-FRF model are unavailable.

Table 5. The sensitivity of using the different methods and data to estimate FRF at 120 bar for sample plotted in Figure 2.

FRF-Model	Used data/method to calculate C_p-C_b	C_p-C_b (bar ⁻¹)	$-\gamma_{Ro}$ (bar ⁻¹)	Rel. Er. (%)
Single	ϕ at 2 OB P./ Equation (13)	1.30E-03	2.82E-03	12.6
Single	ϕ at 4 OB P./ Equation (13)	2.24E-04	4.84E-04	-10.3
Single	Equations (44), (45) & (46)	5.57E-05	1.20E-04	-13.4
Multi	Equation (16)	7.57E-04	1.59E-03	0.4

Conclusions

Based on the developed FRF models and the application of the models to two overburden FRF datasets including sandstone and carbonate samples from seven reservoirs, the following conclusions can be drawn.

1-Two analytical FRF models referred to as the Multi-FRF model and Single-FRF model have been developed. Both exponential models can be converted to linear models for a range of low overburden pressures (for example for net confining overburden pressure $P < 150$ bar for this specific dataset) and include FRF at initial pressure and net confining pressure difference. In addition, the Multi-FRF model involves the rock resistivity modulus, whereas the Single-FRF model is dependent on the cementation exponent, the pore volume compressibility and bulk compressibility. The FRF models have been derived mathematically based on Archie's equation, thus they are expected to be valid within Archie's equation limitation, assumption, and boundary conditions.

2-The validity of the developed FRF models were verified through their applications on 374 actual core data of 79 plug samples (31 sandstone and 48 carbonate plug samples). The results of validation showed that the FRF models succeeded in predicting the behaviour of FRF for the investigated net confining overburden pressure range at ambient temperature with average relative error of 2% and 3% for sandstone and carbonate samples, respectively.

3-Theoretical models are proposed to predict RI, water saturation and saturation exponent behaviour under overburden pressure. In addition, a special Multi-FRF model has been developed to predict apparent FRF for shaly rocks. As RI and C_o/C_w experiments are normally performed only at current reservoir overburden pressure and temperature conditions, the developed models may help to predict RI and F^* behaviours at different overburden pressures - within the model boundary conditions and basic assumptions.

4-However, the model predicted trends, and the maximum change in the saturation exponent with overburden pressure shows consistency with the reported results in literature [24]. Experimental data and further investigations are required to validate the developed theoretical models (RI, S_w , saturation exponent and apparent FRF models).

Acknowledgment

The authors thank Aker BP ASA for granting the permission to publish this paper. Further we thank Reza Askarinezhad (NORCE Norwegian Research Centre AS, Norway) for the original idea that initiated this research paper. Min Cheng (Stratum Reservoir, USA) is acknowledged for fruitful discussions and constructive comments.

Nomenclature

a	Slope of the line in Equation (41), bar ⁻¹
b	Intercept of the line in Equation (41), dimensionless
B	Volume concentration of sodium exchange cations associated with the clay, ($\Omega^{-1}m^{-1}$)/(meq/ml)
C	Salt concentration, g/L
C_b	Bulk compressibility, bar ⁻¹
C_{fb}	Formation brine compressibility, bar ⁻¹
C_o	Brine-saturated rock conductivity, $\Omega^{-1}m^{-1}$
C_p	Pore volume compressibility, bar ⁻¹ (psi ⁻¹ in Equations (44) and (45))
C_w	Brine conductivity, $\Omega^{-1}m^{-1}$
ΔP	Confining pressure difference, bar
ϕ	Porosity, fraction
F^*	Shaly-sand FRF (apparent FRF), dimensionless
FRF	Formation Resistivity Factor, dimensionless
γ_{Co}	Rock conductivity modulus, bar ⁻¹
γ_{Ro}	Rock resistivity modulus, bar ⁻¹
γ_{Rt}	True resistivity modulus, bar ⁻¹
γ_{Rw}	Water resistivity modulus, bar ⁻¹
$HCIIP$	Volume of hydrocarbon initially in place at reservoir conditions, m ³
i	Pressure step
m	Cementation factor
n	Saturation exponent
P	Pressure, bar (psi only in Equation (30))
Q_v	Equivalent conductance of sodium clay exchange cations, meq/ml
RI	Resistivity Index, dimensionless
R_o	Resistivity of rock fully saturated with brine, Ωm
R_t	Resistivity of rock partially saturated with brine, Ωm
R_w	Formation water resistivity, Ωm

S_w	Water saturation, fraction
T	Temperature, °F
V	Volume of the reservoir, m ³
V_b	Bulk volume, m ³
V_p	Pore space volume, m ³
V_w	Volume of the formation brine, m ³

References

- [1] Archie GE. The Electrical Resistivity Log as an Aid in Determining Some Reservoir Characteristics. Transactions of the AIME 1942; 146:54–62. <https://doi.org/10.2118/942054-g>.
- [2] Carter SL, Power HH. The Relationship Between Electrical Resistivity and Brine Saturation in Reservoir Rocks. The Log Analyst 1962;2.
- [3] Mungan N, Moore EJ. Certain Wettability Effects on Electrical Resistivity in Porous Media. Journal of Petroleum Technology 1968; 7:20–5. <https://doi.org/10.2118/68-01-04>.
- [4] Torsæter O, Abtahi M. Experimental Reservoir Engineering Laboratory Workbook. Norwegian University of Science and Technology 2003.
- [5] Masoudi P, Zahedi A, Ali M, Farshid A, Seyed Mohammad Z. Estimation of in Place Hydrocarbon Volume in Multi-Layered Reservoirs Using Deterministic and Probabilistic Approaches. Energy Exploration & Exploitation 2011;29:543–57. <https://doi.org/10.1260/01445987.29.5.543>.
- [6] Fleury M, Efnik M, Kalam MZ. Evaluation of Water Saturation From Resistivity in a Carbonate Field. From Laboratory to Logs. Proceedings of International Symposium of the Society of Core Analysts, SCA2004-22, Abu Dhabi, UAE, 2004, p. 5–9.
- [7] Tiab D, Donaldson EC. Petrophysics: Theory and Practice of Measuring Reservoir Rock and Fluid Transport Properties. Gulf Professional Publishing; 2015.
- [8] Moore EJ, Szasz SE, Whitney BF. Determining Formation Water Resistivity From Chemical Analysis. Journal of Petroleum Technology 1966; 18:373–6. <https://doi.org/10.2118/1337-pa>.
- [9] Dusenbery RA, Osoba JS. Determination of Formation Water Resistivity Using Shale Properties. Permian Basin Oil and Gas Recovery Conference, SPE-150306-MS; 1986. <https://doi.org/10.2118/15030-ms>.
- [10] Henry JD, Cunningham WA. A New Method for Determination of Formation Water Resistivity From the Spontaneous Potential Curve. Fall Meeting of the Society of Petroleum Engineers of AIME, SPE-437-MS; 1962. <https://doi.org/10.2118/437-ms>.
- [11] McPhee C, Reed J, Zubizarreta I. Core analysis: A Best Practice Guide. Elsevier; 2015. <https://doi.org/10.1016/b978-0-444-63533-4.00001-9>.
- [12] Baker RO, Yarranton HW, Jensen J. Practical Reservoir Engineering and Characterization. Gulf Professional Publishing; 2015. <https://doi.org/10.1016/b978-0-12-801811-8.00010-9>.
- [13] Fatt I. Effect of Overburden and Reservoir Pressure on Electric Logging Formation Factor. AAPG Bulletin 1957; 41:2456–66. <https://doi.org/10.1306/0bda59a8-16bd-11d7-8645000102c1865d>.
- [14] Brace WF, Orange AS, Madden TR. The Effect of Pressure on the Electrical Resistivity of Water-Saturated Crystalline Rocks. Journal of Geophysical Research 1965; 70:5669–78. <https://doi.org/10.1029/jz070i022p05669>.
- [15] Timur A, Hemphkins WB, Worthington AE. Porosity and Pressure Dependence of Formation Resistivity Factor for Sandstones. Trans CWLS 4th Formation Evaluation Symp., vol. 30, 1972.
- [16] Jing XD, Archer JS, Daltaban TS. Laboratory Study of the Electrical and Hydraulic Properties of Rocks Under Simulated Reservoir Conditions. Marine and Petroleum Geology 1992;9:115–27. [https://doi.org/10.1016/0264-8172\(92\)90084-r](https://doi.org/10.1016/0264-8172(92)90084-r).
- [17] Longeron DG, Argaud MJ, Feraud JP. Effect of Overburden Pressure and the Nature and Microscopic Distribution of Fluids on Electrical Properties of Rock Samples, SPE Paper 15383. 61st Annual Technical Conference, Society of Petroleum Engineers, New Orleans, LA, October 1986, p. 5–8. <https://doi.org/10.2118/15383-PA>.
- [18] Hashmy KH, Campbell JM. The Effect of Pore Configuration, Pressure and Temperature on Rock Resistivity. SPWLA 7th Annual Logging Symposium, SPWLA-1966-W; 1966.
- [19] Wyble DO. Effect of Applied Pressure on the Conductivity, Porosity and Permeability of Sandstones. Journal of Petroleum Technology 1958; 10:57–9. <https://doi.org/10.2118/1081-G>.
- [20] Glanville CR. Laboratory Study Indicates Significant Effect of Pressure on Resistivity of Reservoir Rock. Journal of Petroleum Technology 1959; 11:20–6. <https://doi.org/10.2118/1153-g>.
- [21] Brace WF, Orange AS. Electrical Resistivity Changes in Saturated Rocks During Fracture and Frictional Sliding. Journal of Geophysical Research 1968; 73:1433–45. <https://doi.org/10.1029/JB073i004p01433>.
- [22] Parkhomenko EI. Electrical Resistivity of Minerals and Rocks at High Temperature and Pressure. Reviews of Geophysics 1982; 20:193–218. <https://doi.org/10.1029/rg020i002p00193>.
- [23] Redmond JC. Effect of Simulated Overburden Pressure on the Resistivity, Porosity and Permeability of Selected Sandstones. The Pennsylvania State University; 1962. <https://doi.org/10.2118/461-pa>.
- [24] Lewis MG, Sharma MM, Dunlap HF. Wettability and Stress Effects on Saturation and Cementation Exponents. SPWLA 29th Annual Logging Symposium, SPWLA-1988-K; 1988.
- [25] Sondena E, Brattell F, Kolltvelt K, Normann HP. A Comparison Between Capillary Pressure Data and Saturation Exponent Obtained at Ambient Conditions and at Reservoir Conditions. SPE Formation Evaluation; SPE-19592-PA 1992; 7:34–40. <https://doi.org/10.2118/19592-PA>.
- [26] Zheng Z, McLennan J, Jones A. Pore Volume Compressibilities Under Different Stress Conditions. SCA-9005, 1990.
- [27] Quist AS, Marshall WL. Electrical Conductances of Aqueous Sodium Chloride Solutions from 0 to 800 d. and at Pressures to 4000 bars. The Journal of Physical Chemistry 1968; 72:684–703. <https://doi.org/10.1021/j100848a050>.
- [28] Behin R. Investigation on the effect of stress on cementation factor of Iranian carbonate oil reservoir rocks. International Symposium of the Society of Core Analysts held in Abu Dhabi, UAE, SCA 2004-41, 2004.

- [29] Eshraghi E, Moghadasi J. An Experimental Investigation on Archie Parameters at Ambient and Overburden Condition of Iranian Clean Carbonate Reservoir Rock and Developing a new Formation Resistivity Model for Limestone and Dolomite Samples. International Petroleum Technology Conference, IPTC-17223-MS; 2014. <https://doi.org/10.2523/IPTC-17223-MS>.
- [30] Osif TL. The Effects of Salt, Gas, Temperature, and Pressure on the Compressibility of Water. SPE Reservoir Engineering 1988; 3:175–81. <https://doi.org/10.2118/13174-PA>.
- [31] Waxman MH, Smits LJM. Electrical conductivities in oil-bearing shaly sands. Society of Petroleum Engineers Journal 1968; 8:107–22. <https://doi.org/10.2118/1863-a>.
- [32] Waxman MH, Thomas EC. Electrical Conductivities in Shaly Sands-I. The Relation Between Hydrocarbon Saturation and Resistivity Index, SPE-1863-A, 213–25. <https://doi.org/10.2118/4094-ms>.
- [33] Zhang S, Zhengwei F. Permeability Damage Micro-Mechanisms and Stimulation of Low-Permeability Sandstone Reservoirs: A Case Study, Bohai Bay Basin, China. Petroleum Exploration and Development 2020; 47:374–82. [https://doi.org/10.1016/S1876-3804\(20\)60054-4](https://doi.org/10.1016/S1876-3804(20)60054-4).
- [34] Aldrich Jr MJ, Lane KS. Pore Pressure Effects on Berea Sandstone Subjected to Experimental Deformation. Geological Society of America Bulletin 1969; 80:1577–86. [https://doi.org/10.1130/00167606\(1969\)80\[1577:ppeobs\]2.0.co;2](https://doi.org/10.1130/00167606(1969)80[1577:ppeobs]2.0.co;2).
- [35] Seyfert CK. Plastic Deformation of Rocks and Rock-Forming Minerals. Structural Geology and Tectonics, Berlin, Heidelberg: Springer Berlin Heidelberg; 1987, p. 495–502. https://doi.org/10.1007/3-540-31080-0_78.
- [36] Schutjens P, Hanssen TH, Hettema MHH, Merour J, de Bree P, Coremans JWA, et al. Compaction-Induced Porosity/Permeability Reduction in Sandstone Reservoirs: Data and Model for Elasticity-Dominated Deformation. SPE-88441-PA, 2004;7:202–16. <https://doi.org/10.2118/88441-PA>.
- [37] Kaye LN, Hacksma JD, Knudson S, Smith JE. Special Core Analysis Loading Conditions for a Friable, Stress-Sensitive Sandstone. Proceedings of 1st Society of Core Analysts European Core Analysis Symposium, London, vol. 21, 1990, p. 23.
- [38] Satter, Abdus, and Ghulam M. Iqbal. Reservoir Rock Properties. Reservoir Engineering, 2016; 29-79. <https://doi.org/10.1016/b978-0-12-800219-3.00003-6>.
- [39] Geertsma, J. The Effect of Fluid Pressure Decline on Volumetric Changes of Porous Rocks. Transactions of the AIME 210.01 1957; 331-340. <https://doi.org/10.2118/728-G>.
- [40] Ahmed, Tarek. Fundamentals of rock properties. Reservoir engineering handbook 2010;189-287. <https://doi.org/10.1016/B978-1-85617-803-7.50012-2>.